

Showcasing research from the Microfluidics and BioMEMS Laboratory of Professor Xinyu Liu, Department of Mechanical and Industrial Engineering, University of Toronto, Canada.

NanoPADs and nanoFACEs: an optically transparent nanopaper-based device for biomedical applications

Nanopaper-based analytical devices (nanoPADs) and nanofibrillated adherent cell-culture platforms (nanoFACEs): a new type of transparent paper-based microfluidic device was developed by using nanofibrillated cellulose paper and applied to chemical/biosensing and cell culture. The transparent device enabled highly sensitive optical detection of biomolecules/chemicals and high-resolution fluorescence imaging of adherent cells, both from the inside of hollow nanopaper channels.


As featured in:



See Xinyu Liu *et al.*,  
*Lab Chip*, 2020, **20**, 3322.


 Cite this: *Lab Chip*, 2020, 20, 3322

## NanoPADs and nanoFACEs: an optically transparent nanopaper-based device for biomedical applications†

 Binbin Ying, <sup>ab</sup> Siwan Park,<sup>c</sup> Longyan Chen,<sup>‡b</sup> Xianke Dong,<sup>ab</sup> Edmond W. K. Young <sup>ac</sup> and Xinyu Liu <sup>\*ac</sup>

Paper has been a popular material of choice for biomedical applications including for bioanalysis and cell biology studies. Regular cellulose paper-based devices, however, have several key limitations including slow fluid flow; large sample retention in the paper matrix for microfluidic paper-based analytical device ( $\mu$ PAD) application; serious solvent evaporation issues, and contamination and poor control of experimental conditions for cell culture. Here, we describe the development of two novel platforms, nanopaper-based analytical devices (nanoPADs) and nanofibrillated adherent cell-culture platforms (nanoFACEs), that use nanofibrillated cellulose (NFC) paper, simply called nanopaper, as the substrate material to create transparent, pump-free and hollow-channel paper-based microfluidic devices. Due to the natural hydrophilicity and nanoscale pore size of nanopaper, the hollow-channel microfluidic devices can realize a totally pump-free flow without any complicated surface chemical functionalization on the nanopaper. Experimental results showed that within a certain range, larger hollow channel size leads to faster pump-free flows. Different from previous designs of paper-based hollow-channel microfluidic devices, the high transparency of the nanopaper substrate enabled the integration of various optical sensing and imaging technologies together with the nanoPADs and nanoFACEs. As proof-of-concept demonstrations, we demonstrated the use of nanoPADs for colorimetric sensing of glucose and surface-enhanced Raman spectroscopy (SERS)-based detection of environmental pollutants and applied the nanoFACEs to the culture of human umbilical vein endothelial cells (HUVECs). These demonstrations show the great promise of nanoPADs and nanoFACEs for biomedical applications such as chemical/bioanalysis and cell biology studies.

 Received 5th March 2020,  
 Accepted 21st July 2020

DOI: 10.1039/d0lc00226g

[rsc.li/loc](http://rsc.li/loc)

## Introduction

Paper has emerged as a popular material of choice in numerous biomedical applications; for instance, it serves as the fluid transport matrix for microfluidic paper-based analytical devices ( $\mu$ PADs)<sup>1–5</sup> and as the culture substrate for cell biology studies.<sup>6,7</sup> Its emergence can be largely attributed to the attractive intrinsic properties of paper, such as its low cost, biocompatibility, biodegradability, amenability to chemical and physical modifications,

disposability, natural wickability and potential for mass manufacture.<sup>3–5,8</sup> Many of these paper-based devices and platforms are made from common porous paper-like substrates that are commercially available (*e.g.*, filter and chromatography paper and nitrocellulose membrane). These substrates can be patterned to form hydrophilic channels or discs through surface modification methods such as wax printing and PDMS coating, which renders them suitable for point-of-care (POC) diagnostics<sup>3,9–13</sup> as well as for cell culture.<sup>6,7</sup> However, paper-based devices have certain limitations. For example,  $\mu$ PADs exhibit slow flow speeds, have large retention of sample solution in the porous paper matrix, and rely on wicking flows that hinder multiphase flows and limit the transport of particulate-carrying solutions.<sup>2,3,14,15</sup> On the other hand, existing paper-based cell culture platforms usually employ disc-shaped paper areas for cell culture (*e.g.*, to match the circular wells of multiwell plates), have difficulty with fluid retention, and encounter challenges with contamination and control of culture conditions.<sup>6</sup>

<sup>a</sup> Department of Mechanical & Industrial Engineering, University of Toronto, 5 King's College Road Toronto, ON, M5S 3G8, Canada.

E-mail: [xyliu@mie.utoronto.ca](mailto:xyliu@mie.utoronto.ca); Tel: +1 416 946 0558

<sup>b</sup> Department of Mechanical Engineering, McGill University, Montreal, QC, Canada

<sup>c</sup> Institute of Biomedical Engineering, University of Toronto, Toronto, ON, Canada

† Electronic supplementary information (ESI) available. See DOI: 10.1039/d0lc00226g

‡ Current address: Division of Engineering, Saint Mary's University, 923 Robie Street, Halifax, Nova Scotia, Canada

To address some of these limitations, other paper-based devices have been developed to include open or hollow microchannels created either by embossing or cutting channels into omniphobic film matrices with transparent adhesive tape sealed on top.<sup>16,17</sup> Although these open-channel designs reduced sample evaporation and enabled fast laminar flows, pumps were needed to drive the liquid within the channels, thus limiting their utility for POC applications. Alternative hollow-channel paper devices have also been developed,<sup>18–20</sup> where a predefined channel in the middle layer of the paper matrix was created by cutting and removing its cellulose matrix. Before bonding, hemichannels were introduced by 3D wax patterning on the bottom layer of paper to confine the liquid in the channel and maintain its hydrophilicity. Fast flow was induced by a single drop of liquid without the need for external pumping, thus allowing for use at the POC.

Despite the current progress on hollow-channel paper devices, these device substrates are still mainly based on commercial cellulose paper that are not optically transparent. The opacity of traditional paper hinders its potential for microfluidic applications that require high optical transparency for light transmission and/or light emission such as for absorption spectroscopy, Raman scattering, and for phase-contrast and fluorescence microscopy to visualize the morphology of cells in culture.<sup>21,22</sup> Recently, an optically transparent hollow-channel device was designed and embossed on a cellophane film for continuous flow electrochemiluminescence (ECL) applications,<sup>23</sup> but this system still required external pumping to drive liquid flow. Furthermore, a hollow-channel paper device with both optical transparency and biocompatibility for cell culture has yet to be demonstrated in combination. Thus, there remains a strong need for a paper that is hydrophilic, can be fabricated into a hollow-channel device and operated without external pumping, and is optically transparent to allow various optical sensing and imaging applications.

Recently, nanofibrillated cellulose (NFC) has emerged as a highly promising substrate material, and has been utilized to fabricate a new type of paper substrate (referred to here as 'nanopaper') for many applications.<sup>24,25</sup> Surface enhanced Raman scattering (SERS), plasmonic, photoluminescent optical sensing platforms, electronic devices and cell culture platforms have been developed using nanopaper or its gel type as a substrate.<sup>25–28</sup> Similar to cellulose filter paper, nanopaper is hydrophilic, biodegradable, flexible, and inexpensive.<sup>29,30</sup> In addition, nanopaper is also optically transparent because of its nanometer-sized NFC fiber diameter, nanoscale pore size, and ultrasoft surface.<sup>25</sup> These characteristics enable nanopaper to be considered an appropriate substrate candidate for constructing hollow-channel paper devices. For example, a pump-free, closed-chamber microfluidic channel device was assembled by sandwiching two polyethylene terephthalate (PET) substrates containing patterned dried NFC slurry with a thick spacer

forming an air gap in between.<sup>31</sup> However, this dried NFC slurry lacks optical transparency in this design. In contrast, people succeeded in constructing hollow channels by 3D printing petroleum-jelly ink inside a transparent NFC hydrogel matrix; after NFC hydrogel dried in the ambient environment, the printed ink was melted and removed by applying compressed air through the channels.<sup>32</sup> Here, 3D printing created a new strategy to fabricate transparent hollow-channel paper devices, especially for the construction of complex 3D channels. However, using 3D printing to construct hollow channels in this design is incompatible with conventional fabrication schemes for creating paper-based devices, and is relatively troublesome as ink removal in the channels involves the use of toxic chemicals. In addition, to prevent liquid penetration through the channel surface, the hydrophobic coating of a thin layer of silicone elastomer in the channel inner surface means that this design still requires external pumping. To date, a transparent hollow-channel paper device that is low-cost, easy to fabricate, naturally pump-free, and biocompatible is still highly desirable to better meet the requirements of POC diagnostics and cell culture.

In this paper, we describe, for the first time, the use of prefabricated nanopaper as a novel substrate to construct highly transparent, pump-free and biocompatible nanopaper-based analytical devices (nanoPADs) and nanofibrillated adherent cell-culture platforms (nanoFACES). To create these paper-based devices, we stacked multiple layers of nanopaper and bonded them together using either ethylene vinyl acetate (EVA) or biocompatible collagen as the bonding material (Fig. 1a). We manufactured hollow channels in the device by using laser cutting, a common and facile fabrication technique. Due to the selection flexibility of adhesion material for bioanalytical assays, the adhesive for nanoPADs assembly can be selected from a wide range of materials including 3M transparent adhesion, EVA film as well as collagen. While assembling nanoFACES, we must consider biocompatibility of the adhesive to cell culture. Collagen was selected as the adhesive for nanoFACES bonding due to their good sealing performance as surgical adhesives and sealants<sup>33–37</sup> and their biocompatibility for cell culture.<sup>38,39</sup> Each layer of a nanoFACE was assembled into a microfluidic device using polymerized collagen gel as a biocompatible adhesive. This design enabled the efficient fabrication of transparent microchannels while avoiding lateral fluid leakage. As the surface of nanopaper is naturally hydrophilic, liquid wicked into hollow channels without any external pumping. By adjusting the channel width and height, we studied their flow profiles. As proof-of-concept demonstrations, we demonstrated their utility for: (i) simple colorimetric assays for glucose detection, (ii) SERS-based chemical sensing with a gold (Au) Raman substrate decorated inside the hollow channels for environmental pollution monitoring, and (iii) on-chip culture of human umbilical vein endothelial cells (HUVECs) for vascular research.

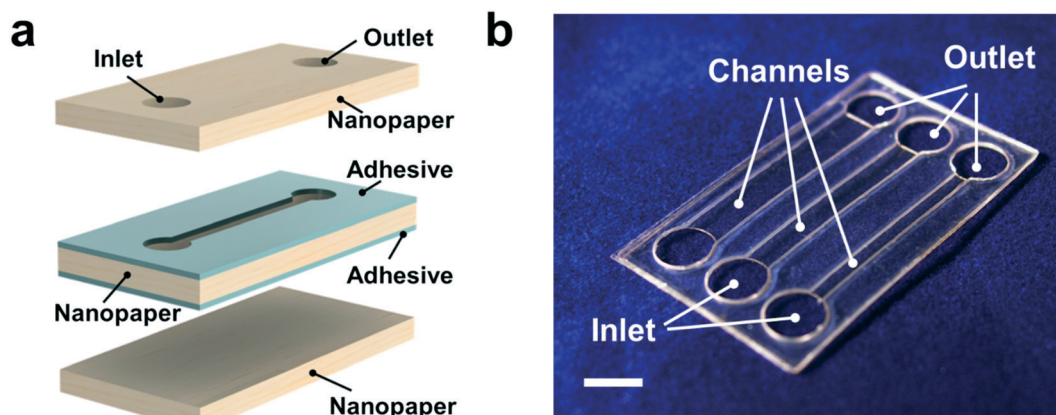


**Fig. 1** Fabrication of hollow-channel devices. (a) Schematic design of a hollow-channel device for nanoPADs and nanoFACES. EVA or collagen was used as the adhesive/bonding material depending on application requirements. (b) Photograph of a transparent nanoPAD (EVA-bonded) with 3 channels (1 mm, 2 mm, and 3 mm wide). Scale bar: 4 mm.

## Materials and methods

### Reagents and materials

(2,2,6,6-Tetramethylpiperidin-1-yl)oxidanyl (TEMPO)-oxidized NFC (slurry, 1.0 wt% solid) was purchased from the Process Development Center at the University of Maine. EVA film was obtained from Tianjin Caida New Materials Technology Co., Ltd. (Tianjin, China). Teflon® film made from Teflon® polytetrafluoroethylene (PTFE) and polyethylene terephthalate (PET) were ordered from McMaster-Carr (Elmhurst, IL, USA). The reagents employed in glucose colorimetric tests were purchased from Sigma-Aldrich (Oakville, ON, Canada). Gold(III) chloride trihydrate ( $\text{HAuCl}_4$ , >99%), Rhodamine B (RhB, >95%), 4-(2-hydroxyethyl) piperazine-1-ethanesulfonic acid, *N*-(2-hydroxyethyl) piperazine-*N'*-(2-ethanesulfonic acid) (HEPES, >99.5%) and phosphate buffered saline solution (PBS, 10 $\times$ ) were purchased from Sigma-Aldrich (St. Louis, MO, USA). All the reagents were directly used without further purification.

### Nanopaper preparation

In a typical experiment, the TEMPO-oxidized NFC slurry was dispersed in deionized water (18.2 M $\Omega$  cm, Milli-Q Gradient System, Millipore) to a final concentration of 0.1 wt%, and the suspension was stirred at 1000 rpm for 2 h. Two hundred grams of the above suspension was vacuum-filtered for 20 h with a hydrophilic PVDF filter membrane (VVL09050, EMD Millipore Corporation, pore size: 0.1  $\mu\text{m}$ ) on a glass filter holder (XX1009020, EMD Millipore Corporation). After filtration, a wet transparent gel was formed on top of the filter membrane. The “gel cake” (7 cm in diameter) was peeled off from the filter membrane, then carefully stacked between two plastic rings and stored in the 40 °C oven for 1 h for partial drying. Next, the partially dried nanopaper was placed between two Teflon films and hot-pressed under a pressure of 2.6 MPa at a high temperature for 10 min to form a completely dried and flat nanopaper substrate. The

thickness of a typical nanopaper used in our experiments was 80  $\mu\text{m}$  unless otherwise noted.

### Synthesis of gold nanostars

Highly branched Au nanostars (AuNSs) were synthesized using a previously reported one-step method.<sup>40</sup> Briefly, 100 mM solution of HEPES was prepared in DI water and its pH was adjusted to 7.4 by using 1 M NaOH. Next, 2 ml of HEPES solution was mixed with 3 ml of DI water and 50  $\mu\text{L}$  of 20 mM solution of gold(III) chloride hydrate solution in a glass vial. The vial was kept at room temperature for 60 min without stirring. The color of the mixture changed from light yellow to colorless, to light pink, and finally to dark blue over a period of 20 minutes. The reaction was further aged for 1 h. Afterwards, the sample was washed and centrifuged twice. The as-made AuNSs were kept in dark environment at room temperature for subsequent use.

### Characterization

The morphology of NFC was acquired by using a Philips Technai G2 20 transmission electron microscope (TEM, FEI, US) equipped with a Gatan imaging filter operating at 120 kV. The NFC sample for TEM characterization was prepared as follows: 5  $\mu\text{L}$  0.1 wt% NFC suspension was first dropped on a positively charged TEM grid, which was dried using filter paper after 2 min. Next, these grids were stained by depositing 2  $\mu\text{L}$  of a 0.1% w/v solution of poly-L-lysine and 2  $\mu\text{L}$  0.4% w/v solution of uranyl acetate successively. These solvents were removed with a filter paper after 2 min. Similarly, 2  $\mu\text{L}$  AuNS sample was deposited on a regular TEM grid and dried in air for TEM characterization of the AuNS size and shape.

The transmittance of nanopaper and absorption spectra of gold nanostars were obtained with a UV-vis spectrometer (SpectraMax M5, Molecular Devices, Sunnyvale, CA). An ultrafast atomic force microscope (AFM) (JPK Nanowizard® 3, Berlin, Germany) was used to characterize the surface of the nanopaper.

Tensile test was conducted to determine the mechanical strength of the nanopaper with a universal testing machine (MTEST-Quattro, ADMET, the loading cell is 1 kN). A rectangular strip (5 mm × 50 mm) was prepared for the tensile test. The strain rate was fixed at 20% min<sup>-1</sup>. The tensile strain ( $\epsilon$ ) was defined as the length change ( $\Delta l$ ) divided by the original length ( $l_0$ ) of the sample.

#### Reagent preparation for glucose colorimetric detection

D-(+)-Glucose (99.5%) was used as a model analyte in the colorimetric test. The colorimetric reaction for detecting glucose was based on the oxidation of this analyte by glucose oxidase with hydrogen peroxide produced. Thereafter, the color of oxidation indicator changed due to the oxidation reaction with the generation of hydrogen peroxide. Accordingly, oxidase solution was prepared by mixing 120 U mL<sup>-1</sup> glucose oxidase (from *Aspergillus niger*, 147.9 U mg<sup>-1</sup>) and 30 U mL<sup>-1</sup> peroxidase type I (from horseradish, 50 U mg<sup>-1</sup>). 0.3 M trehalose was used as stabilizer. The oxidation indicator was prepared by mixing 0.2 M 4-aminoantipyrene and 0.4 M 3,5-dichloro-2-hydroxy-benzenesulfonic acid.

Glucose was diluted in the artificial urine solution at different concentrations for detection. The preparation of artificial urine solution was reported previously.<sup>41–43</sup> The artificial urine solution contained 2.5 mM calcium chloride, 2 mM citric acid, 90 mM sodium chloride, 1.1 mM lactic acid, 2 mM magnesium sulfate, 10 mM sodium sulfate, 7 mM potassium dihydrogen phosphate, 170 mM urea, 25 mM sodium bicarbonate, 7 mM dipotassium hydrogen phosphate, and 25 mM ammonium chloride. The pH of the solution was adjusted to 6 by using 1 M hydrochloric acid.

#### SERS measurement

All Raman spectra were measured using a confocal Raman spectroscope (inVia™, Renishaw) equipped with a 633 nm laser source and a charge-coupled device (CCD) detector. After a sample was introduced into the inlet of a hollow channel, the Raman substrate coated with the concentrated AuNSs was focused using 50× objective lens. The signals were collected with 10 mW laser power for 10 s exposure time. Subsequently, the Raman spectrum was acquired in the wavenumber range of 400 to 1800 cm<sup>-1</sup> with a spectral resolution of 1 cm<sup>-1</sup>. A baseline correction routine was performed on the spectral data to obtain the final spectrum with the background subtracted. All the spectral data were analyzed using Origin Lab software.

#### Biocompatibility

The biocompatibility of nanopaper was characterized as follows: human umbilical vein endothelial cells were cultured in endothelial growth medium BulletKit (EGM, #CC-3124, Lonza) consisting of endothelial basal medium (EBM, CC-3121) mixed with EGM SingleQuots Supplements (CC-4133). For each experiment, HUVECs at passage 5 were used for consistency. Cultured cells were trypsinized from the culture

flask and a density of 10 000 cells per cm<sup>2</sup> were seeded in the polystyrene 96-well plate (SARSTEDT AG, Germany) with four different substrates or substrate coatings: (i) polystyrene (PS), (ii) PS with human plasma fibronectin (FN, Sigma-Aldrich) coating (100 µg mL<sup>-1</sup> for 30 min at 37 °C) (iii) nanopaper, and (iv) nanopaper with FN coating (100 µg mL<sup>-1</sup> for 30 min at 37 °C). Round nanopaper discs were prepared with a 6 mm biopsy punch and placed in the wells of a 96-well plate to be used as a cell culture substrate. HUVECs in the wells were cultured for 48 h from initial seeding and the culture medium was replenished after 24 h. After 48 h, HUVECs were fixed using 4% paraformaldehyde (PFA) and permeabilized with 0.1% Triton X-100. 1% BSA was used as a blocking buffer to prevent non-specific binding. F-actin was stained with Alexa Fluor 488 phalloidin (Invitrogen) and nuclei were stained with Hoechst. Microscopic images were taken from an EVOS FL-Auto microscope (Thermo Fisher Scientific). ImageJ software was used to measure the percentage of area covered by the HUVECs. Images of the wells were converted to 16-bit images. Then, the background was subtracted with a rolling ball radius of 15 pixels, and the color threshold was adjusted to remove the background from the cells. Finally, the area covered by the cells in percentage was measured. The confluency experiment was performed three times ( $n = 3$ ) and each independent experiment contained up to four replicates for each condition. One-way ANOVA with *post hoc* Tukey test was used to determine the significance difference between conditions.

#### Cell culture on nanoFACES

A complete hollow-channel nanoFACE was assembled with 5 layers of 80 µm thick nanopaper with laser-cut channel openings. The bonding of each layer was achieved using collagen gel as an adhesive matrix. The collagen solution (5 mg mL<sup>-1</sup>, pH 7.4) was prepared by mixing 0.5 N NaOH, phosphate buffer saline (PBS), and high-concentration type I collagen (rat-tail, Corning, #354249). Nanopaper layers were stacked on top of each other with applications of collagen solution between them. Excess collagen solution in the channel was removed by aspiration. The device was immediately placed in the 37 °C incubator for 30 minutes for the polymerization of collagen. After incubation, channels were coated with human plasma fibronectin (100 µg mL<sup>-1</sup>) for 30 minutes at room temperature to facilitate cell adhesion.

HUVECs in EGM media were suspended at a density of 2 × 10<sup>6</sup> cells per ml and were drawn into the channel by only capillary force thereafter. An extra volume of culture media was added on top of the inlet port within 15 to 30 minutes of initial seeding to prevent dehydration. The nanoFACE was placed in the incubator (37 °C and 5% CO<sub>2</sub>) for 12 h before imaging.

## Results and discussion

#### Characterization of NFC and nanopaper

We first studied the morphology of NFC by TEM imaging. The diameter of NFC used in our nanopaper was ~10 nm and uniformly distributed, while the length of most NFC was

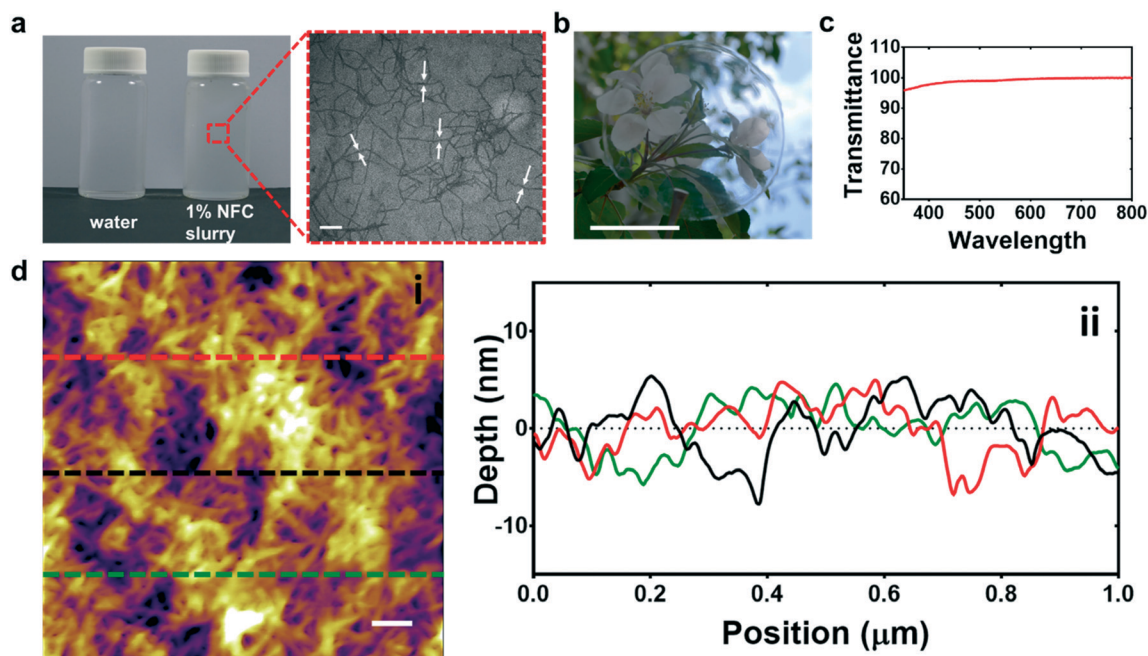


**Fig. 2** Characterization of NFC and nanopaper. (a) NFC slurry solution in bottles and TEM image of NFC. Scale bar: 100 nm. (b) Photograph of an 80  $\mu\text{m}$ -thick nanopaper processed by hot-pressing at 85  $^{\circ}\text{C}$ . Scale bar: 35 mm. (c) Transmittance data of the nanopaper in Fig. 2b. (d-i) An AFM image showing the nanopaper roughness in a 1  $\mu\text{m}$   $\times$  1  $\mu\text{m}$  area. Scale bar: 100 nm. (d-ii) Surface roughness depth data along the three scanning lines of the AFM image in (d-i).

over 500 nm, as shown in Fig. 2a. The TEMPO-mediated oxidation replaced primary hydroxyl groups of cellulose to carboxylate ones and made TEMPO-oxidized NFC homogeneously dispersed in water,<sup>44–46</sup> which is important to fabricate nanopaper with uniform NFC fiber distribution. Next, we explored the optimal condition to fabricate a highly transparent nanopaper by filtrating 0.1 wt% NFC slurry and hot pressing the “gel cake”. Because the introduction of carboxyl group into cellulose can reduce the thermal decomposition temperature of nanopaper,<sup>47</sup> higher temperatures can lead to yellowing of the nanopaper. Therefore, we first studied the optimal temperature of hot pressing to manufacture a transparent nanopaper. Hot pressing temperatures below 75  $^{\circ}\text{C}$  were not chosen here because the partially dried nanopaper (after 1 h baking at 40  $^{\circ}\text{C}$ ) cannot be dried completely by hot pressing at  $<75$   $^{\circ}\text{C}$  for 10 min. Therefore, we mainly studied the temperature range from 75  $^{\circ}\text{C}$  to 100  $^{\circ}\text{C}$ . The transmittance of nanopaper hot-pressed at 75  $^{\circ}\text{C}$  or 85  $^{\circ}\text{C}$  for 10 min is over 95% in the wavelength range of 350–800 nm while higher temperatures ( $\geq 100$   $^{\circ}\text{C}$ , 10 min) can lower the transmittance to 73% of the original value at 85  $^{\circ}\text{C}$  (Fig. 2c and S3†) due to the decarbonation of anhydroglucuronate units. Herein, we chose 85  $^{\circ}\text{C}$  as the hot-pressing temperature for preparing the nanopaper for device construction.

Fig. 2b illustrates a transparent nanopaper processed at 85  $^{\circ}\text{C}$  after 10 min hot pressing. The nanopaper thickness was measured to be 80  $\mu\text{m}$ . One can adjust the weight percentage of the NFC suspension for filtration to form nanopaper with different thicknesses. The high transparency

of the nanopaper is due to its nanometer-sized NFC fiber diameter, nanoscale pore size, and ultrasmooth surface (Fig. 2d). Light can pass through a thin nanopaper substrate with little light scattering effect.<sup>25</sup> This key property allows hollow-channel nanoPADs and nanoFACES to be potentially integrated with various optical sensing and imaging applications. In addition, due to the large surface area of NFC, the nanopaper showed a high Young’s modulus (10.02 GPa) and high flexibility with a small bending radius (3 mm) (Fig. S2†). These excellent mechanical properties are close to those of NFC paper reported previously.<sup>48,49</sup>

We then characterized the optical stability of nanopaper by conducting an accelerated aging test and measuring its transparency over different durations of thermal degradation (at 75  $^{\circ}\text{C}$ ). The transparency showed a decrease of 1.6% after 1 h and 2.5% after 16 h, respectively (Fig. S4a†). Real-time stability was calculated according to ASTM F1980 (ambient temperature: 23  $^{\circ}\text{C}$ ; aging factor  $Q_{10}$ : 2).<sup>50</sup> Consequently, our nanopaper can maintain its high transparency for at least 24.5 days. This transparency maintenance was further confirmed by an optical photograph taken one month after nanopaper was fabricated (Fig. S4b†). We also characterized the surface topography of nanopaper by AFM as it is another important characteristic for device applications. By randomly selecting a 10 mm  $\times$  10 mm piece of nanopaper from an as-fabricated sample, we conducted AFM scanning in a 1  $\mu\text{m}$   $\times$  1  $\mu\text{m}$  area with 512  $\times$  512 sampling points. The maximum surface roughness depth from a randomly selected scan line (black line in Fig. 2d) was determined to be 9.66 nm and its root mean square (RMS) roughness was 2.58 nm. This low

surface roughness is comparable to that of other similar studies<sup>26,51</sup> and could enable a faster flow speed and transport particulate-carrying solutions. Next, we characterized the capability of liquid penetration along the thickness of nanopaper. Red food dye was used as the liquid for visualization. We found that the dye only penetrated ~13.6% of the paper thickness (80  $\mu\text{m}$ ) in the first 10 min and the relative penetration depth stopped at 22.1% from 20 min to 60 min. The slow penetration is due to the nanoscale pore size of the nanopaper substrate.<sup>25,52</sup> We can take advantage of this feature to confine the liquid in the hollow channel without any further surface modification (*i.e.*, wax printing). Additionally, nanopaper is resistant to various solvents (*e.g.*, water, methanol, toluene, and dimethylacetamide),<sup>53</sup> and the homogeneous carboxylate groups on the surface enable tight covalent bonding to proteins, DNA, and other biomolecules by surface modification.<sup>54</sup> Therefore, the nanopaper is an excellent substrate to construct nanoPADs for chemical and biological detection.

### Fabrication of transparent hollow-channel devices

A schematic of our hollow-channel device design is shown in Fig. 1a. The device is comprised of three layers of nanopaper to construct the hollow channel structures and two adhesive layers to attach the three nanopaper layers together. Inlets and outlets in the top nanopaper layer and hollow channels in the middle nanopaper layer were designed using Solidworks and cut by a CO<sub>2</sub> laser cutter (VLS 2.30, Universal Laser Systems, Scottsdale, AZ, USA). Thereafter, we used methanol/alcohol to wash the nanopaper for drying overnight before assembly to remove the laser cutting ash, and the nanopaper was found to be still rigid and transparent after washing. The height of the hollow channels can be adjusted by changing the thickness of the middle nanopaper layer or by stacking multiple middle layers of nanopaper.

For nanoFACES, collagen was applied to be an effective adhesive matrix because of its biocompatibility and its ability to bond to the nanopaper surface without leakage. Most importantly, the polymerized collagen was able to prevent warping of the nanopaper with its adhesiveness and rigidity during long-term humidity exposure. 20  $\mu\text{l}$  of 5 mg ml<sup>-1</sup> type I collagen solution at pH 7.4 was subsequently drop-coated on top of each nanopaper layer during layer-by-layer stacking. After aspirating the excess collagen from the hollow channel, the entire device construct was polymerized in an incubator (37 °C, 5% CO<sub>2</sub>) to provide structural integrity for the device. As a result, no lateral leakage of cells into the collagen bonding area was observed during experiments because the strong protein–nanocellulose interaction held the entire device together firmly.<sup>55</sup> From Fig. S6† we further found that bonded hollow-channel nanoFACES still maintained good optical transparency, which is due to both the transparency of the polymerized collagen and the intimate bonding between the collagen and the nanopaper.

For nanoPAD assembly, we selected EVA as the bonding material and used thermal bonding to assemble different nanopaper layers. EVA has been reported as an excellent material for glass lamination without loss of optical transparency.<sup>56,57</sup> A 40  $\mu\text{m}$ -thick EVA film was used in our experiment. After alignment and assembly according to the schematic design, the device was pressed between two glass slides with four clips and stored in the oven at 75 °C to develop a strong adhesion (the melting point of the EVA we chose was 65 °C). We found that the device was firmly bonded after 1 h of thermal bonding. Fig. 1b shows a transparent hollow-channel nanoPAD assembled through EVA bonding. The channel height was ~160  $\mu\text{m}$  and channel widths were 1 mm, 2 mm and 3 mm. Smaller channel widths (*e.g.*, 500  $\mu\text{m}$ ) can also be fabricated by laser cutting if needed. Notably, the transparency of the bonding part remained at 96.5% of that of the nanopaper after thermal bonding for 1 h, suggesting that the EVA-based thermal bonding is effective for constructing highly transparent nanoPADs. Conservation of high device transparency after EVA bonding can be explained by the fact that during thermal bonding the melted EVA can fill into the nanoscale pores of the nanopaper to allow light to pass through the bonding layer without significant loss. No lateral leakage into the bonding area was observed in all our flow tests (Movie S1†). Therefore, EVA proved to be a good adhesion material for bonding nanoPADs.

### Wicking performance characterization

The designed hollow channel structure on nanopaper enabled a much faster pump-free flow speed than that in regular cellulose paper channels (Movie S1†) and a comparable flow speed to that of conventional paper-based hollow-channel devices.<sup>18</sup> We characterized the flow wicking performance inside the hollow-channels of EVA-bonded nanoPADs. During the tests, all channels were vertically arranged above an aqueous solution reservoir (Movie S1†), which eliminated the effect of the gravity- and surface-tension-induced pressure of the liquid drop at the channel inlet. We found that the aqueous solution was driven into the channels only by capillary force originating from the hydrophilic inner walls of the hollow channel. The wicking flow speed was not constant along the channel length and decreased with the travel distance of the flow front into the channel (Fig. 3a). This finding is theoretically supported by the Lucas–Washburn equation:<sup>58</sup>

$$v(t) = \sqrt{\frac{\gamma \cdot r \cdot \cos \theta}{8\mu \cdot t}} = \sqrt{\frac{\gamma \cdot \cos \theta}{8\mu \cdot t \left(\frac{1}{h} + \frac{1}{w}\right)}} \quad (1)$$

where  $v(t)$  is the speed of the advancing liquid front under capillary pressure into a channel;  $t$  is time;  $\gamma$  is the surface tension;  $\theta$  is the contact angle;  $\mu$  is the dynamic viscosity of the liquid;  $r$  is the effective capillary radius of the rectangular channel and  $r = 1/\left(\frac{1}{h} + \frac{1}{w}\right)$ ;  $h$  is the channel height; and  $w$  is the channel width. Eqn (1) was derived with several

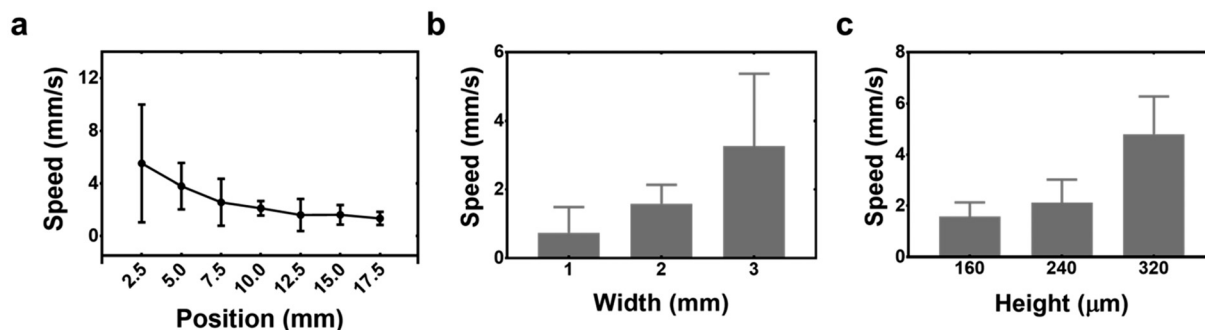


**Fig. 3** Characterization of flow wicking performance inside hollow channels. (a) Flow wicking speed along the hollow channel ( $N = 3$ ). The position of  $x$ -axis refers to the distance from the channel inlet. Channel width: 2 mm. (b) Flow wicking speed (at the position of 10 mm) in channels of different widths ( $N = 3$ ). Channel height: 160  $\mu\text{m}$ . (c) Flow wicking speed (at the position of 10 mm) among channels with different heights ( $N = 3$ ). Channel width: 2 mm.

assumptions including that gravity and inertial forces were negligible in a micro-scale channel and the driving force of the liquid rising was mainly from the capillary pressure.<sup>59</sup> According to eqn (1), the wicking flow speed decreased with time when the fluid front rose. However, the flow speed in the hollow channel is fast enough to efficiently carry out bioanalytical assays with negligible evaporation.<sup>18</sup> We then studied the impact of the channel size on the wicking performance. The wicking speed became faster when channel width or height increased (Fig. 3b and c), which is predictable according to the Lucas–Washburn capillary model with viscous effects.<sup>58</sup> Since the contact angle  $\theta$ , surface tension  $\gamma$  and viscosity  $\mu$  in eqn (1) are all constant, a larger capillary force and thus a faster wicking speed were present in a wider/higher channel due to its larger effective capillary radius  $r$ . For example, as the channel width increased from 1 mm to 3 mm, the flow speed at the position of 10 mm from the inlet rose from 0.735  $\text{mm s}^{-1}$  to 3.258  $\text{mm s}^{-1}$  (Fig. 3b). These characterization results can be leveraged to design hollow channels with desired flow speeds.

### NanoPADs for glucose colorimetric detection

The high transparency of nanoPADs enables the observation of chemical and biological reactions inside hollow channels. Herein, we demonstrated colorimetric detection of glucose on the nanoPADs. We first wicked 3  $\mu\text{L}$  of 1 $\times$  PBS solution spiked with glucose detection reagents (glucose oxidase, stabilizer and oxidation indicator) into a hollow channel of 2 mm wide, 5 mm long, and 160  $\mu\text{m}$  high (Fig. 4a), and dried the reagent solution at room temperature for 10 min. Then, we added 3  $\mu\text{L}$  of artificial urine spiked with glucose at different concentrations into the channel to enable the reaction. Fig. 4b shows a photograph of five hollow channels with urine samples added at different glucose concentrations (4–20 mM) after 10 min reaction. We observed that the intensity of the reddish color produced from the glucose assay was uniform in the entire transparent channel and increased with glucose concentration. The colorimetric assay

results were reproducible, which is evidenced by its small coefficients of variation (CV: standard deviation of the color intensity divided by its mean; Table S1†). The photograph of the assay channel after 10 min reaction was scanned by a desktop scanner (LiDE 210, Cannon, Japan), and the average grayscale intensity of each channel was quantified using ImageJ®. Fig. 4c shows the linear calibration curve of our nanoPADs for glucose detection in the clinically relevant range of 0–20 mM. We found that the grayscale color intensity had a linear relationship with the concentration of glucose between 0 to 20 mM with a sensitivity (the slope value of its calibration curve) of 2.85 ( $R^2 = 0.98$ ). The limit of detection (LOD) of our nanoPAD for glucose detection was calculated to be 1.4 mM, which was defined as the glucose concentration corresponding to the blank control intensity plus three times of the standard deviation of the color intensities from the blank control. These results confirmed that our nanoPADs possess similar analytical performance as that of previously reported  $\mu\text{PADs}$ .<sup>41</sup> In the future, we envision extending the nanoPADs-based colorimetric assay to multiplexed detection of other analytes such as uric acid and lactate.

### NanoPADs for SERS-based chemical sensing

The high transparency of nanoPADs can also enable other types of optical detection inside the channel. In this work, we demonstrated SERS-based chemical detection on our nanoPADs. Gold nanostars were selected as the Raman metal substrate, which has been demonstrated for high-sensitivity chemical detection with strong Raman signal enhancement and long-term stability.<sup>60</sup> The morphology of AuNSs we synthesized was uniformly distributed with a diameter of  $\sim 50$  nm (inset of Fig. 5a and S8†). The tips of the AuNSs allowed enhancement of the Raman signal. Before thermal bonding of a nanoPAD, 2  $\mu\text{L}$  of concentrated AuNSs solution was added to the bottom circle area of the hollow channel (diameter: 4 mm) as the Raman substrate (Fig. 5a). In our demonstration, a commonly used Raman reporter [Rhodamine-B (RhB)] was selected as the target chemical and



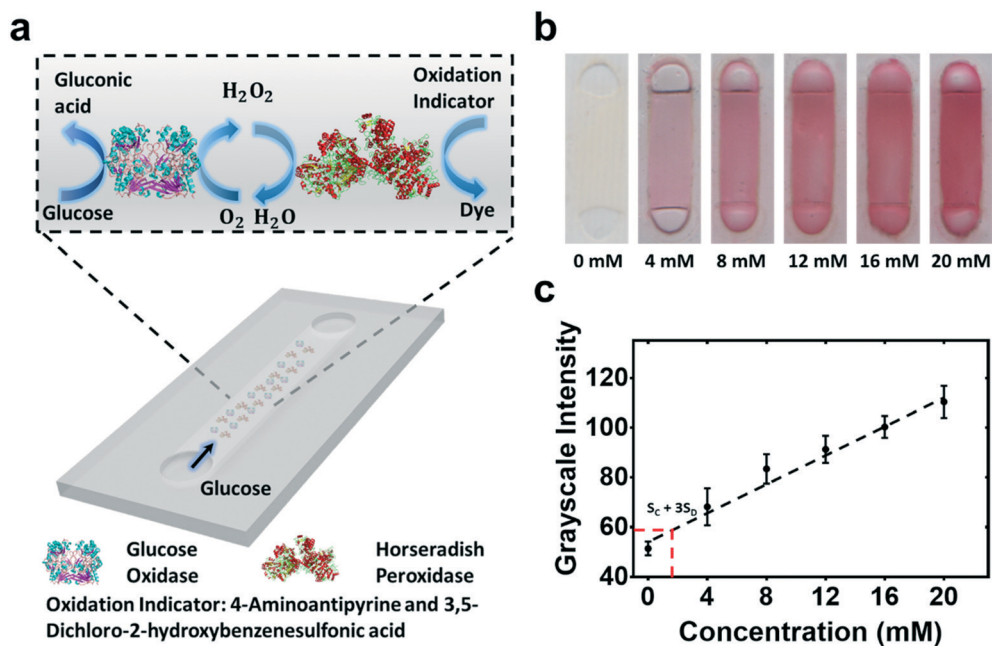


Fig. 4 NanoPADs for glucose colorimetric detection. (a) Schematic of a nanoPAD for glucose colorimetric detection. (b) Colorimetric signals in hollow channels after 10 min reaction at different glucose concentrations. Channel width: 2 mm. (c) Experimental results of the colorimetric grayscale intensity as a function of the glucose concentration ( $N = 4-5$ ). The dashed line represents a linear curve fit to the intensity-concentration data with a regression equation:  $y = 55.7 + 2.85x$  ( $R^2 = 0.98$ ).

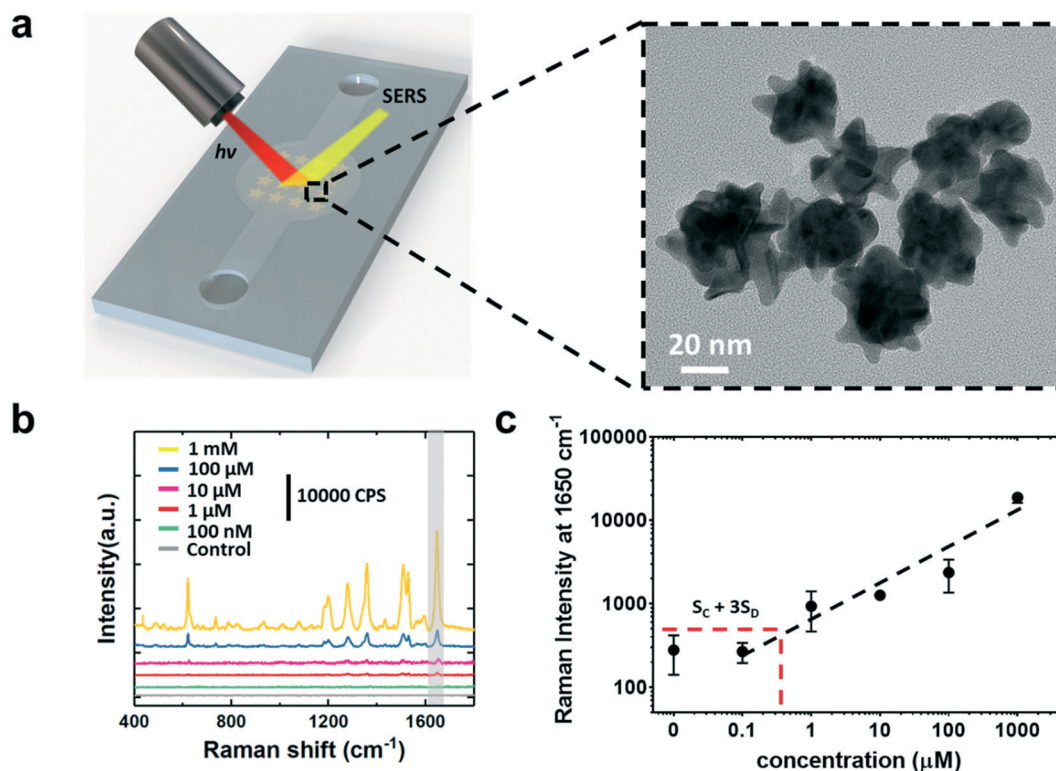


Fig. 5 NanoPADs for SERS-based chemical detection. (a) Schematic of the nanoPAD-based SERS platform; the inset shows a TEM image of Au nanostars (AuNSs) as the Raman substrate. Scale bar: 20 nm. (b) Raman spectra of RhB solutions at concentrations of 0–1 mM in hollow channels. (c) Calibration curve of RhB detection by reading the Raman signals at  $1650 \text{ cm}^{-1}$  ( $N = 4-5$ ). The fitted linear curve in the range of 0.1  $\mu\text{M}$  to 1000  $\mu\text{M}$  was  $\log y = 0.41 \log x + 2.84$  ( $R^2 = 0.9$ ).

artificial environmental pollutant. 4  $\mu\text{L}$  of RhB aqueous solution was wicked into the hollow channel, and the Raman signal was then quantified thereafter. Each signal acquisition took around 1 min. During analyte solution wicking, AuNSs were found to attach well on the nanopaper substrate, indicating that physisorption (*e.g.*, hydrogen bonds) between nanopaper and HEPES-stabilized AuNSs can at least withstand fluid shear in our current capillary flow speed range. However, to ensure their attachment to the nanopaper under much faster microfluidic speeds, the AuNSs can be bonded to nanopaper by covalent linkers to form a more robust AuNS SERS substrate on nanopaper. For example, the surface of AuNSs can be functionalized by primary amine groups ( $-\text{NH}_2$ ) and form amide bond ( $-\text{COO}-\text{NH}-$ ) with the carboxyl groups ( $-\text{COO}^-$ ) on nanopaper.<sup>61,62</sup> Fig. 5b shows Raman spectra of the RhB samples at different concentrations (100 nM–1 mM). These spectra revealed all the prominent characteristic Raman bands of RhB at 1278  $\text{cm}^{-1}$ , 1355  $\text{cm}^{-1}$ , 1603  $\text{cm}^{-1}$ , and 1650  $\text{cm}^{-1}$ . The characteristic Raman peak of RhB at 1650  $\text{cm}^{-1}$  (the aromatic C–C stretching mode) was selected as the readout signal of RhB detection. As shown in Fig. 5c, the calibration curve of the 1650  $\text{cm}^{-1}$  Raman peak value *vs.* the RhB concentration revealed a linear relationship in the logarithmic scale from 0.1  $\mu\text{M}$  to 1000  $\mu\text{M}$  ( $R^2 = 0.9$ ). The LOD of our nanoPADs for RhB detection was calculated to be 0.8  $\mu\text{M}$ , which was defined as the RhB concentration corresponding to the blank control intensity plus three times the standard deviation of the Raman intensities from the blank control. Although the transparency (90–95% in the wavelength range of 300–900 nm) of nanopaper could have a slight effect on the acquisition of Raman signal and may lead to a loss of LOD (5–10%), this transparency is similar to that of other conventional SERS-microfluidics on glass or PDMS platforms<sup>63,64</sup> and is enough for high-resolution optical sensing applications. On the other hand, the LOD could be further improved by increasing the sharpness of AuNS tips to the extent comparable to a previous report,<sup>60</sup> which could further increase the Raman signal enhancement near the “hot spots”. Currently, drop-casting technique was utilized for coating a SERS substrate on nanopaper due to its simplicity. However, the uniformity of the plasmonic AuNS layer remains a challenge, resulting in the variation of SERS signals on one substrate.<sup>65,66</sup> For example, the coffee ring effect is a common drawback for drop-casting of metal nanomaterials on paper substrate.<sup>65,67</sup> There are several methods developed to ensure both signal uniformity and enhancement level. For example, a highly dense Ag nanoparticle layer can be synthesized on nanopaper utilizing the surface carboxyl groups,<sup>26</sup> in which the synthesized SERS substrate can ensure both signal homogeneity and enhancement level.

Furthermore, SERS has been widely recognized as one of the most attractive analytical methods for selective detection of biological and chemical analytes in a label-free manner due to the small bandwidth of the molecular fingerprints in

the Raman spectrum.<sup>66</sup> Therefore, the specific detection of a certain analyte in a complex solution matrix on our nanoPADs needs to be demonstrated in the future, which will eventually enable real sample analysis (*e.g.*, food testing) on our nanoPADs. Currently, due to the background complexity of a real sample (*e.g.*, milk and fruit juice), it remains challenging for specific detection of an analyte (*e.g.*, contaminant) from a complex sample due to the overlap of Raman fingerprints of the analyte and the sample background. Accordingly, researchers have come up with several methods including advanced analysis using machine learning algorithms, dilution of the background solution, functionalization of antibodies and aptamers onto SERS substrates for specific capture.<sup>66</sup>

### NanoFACES for cell culture

The main purpose of nanoFACES is to serve as a potential platform for cell culture. Therefore, a simple cell adhesion assay of nanopaper was first performed to determine the cell adhesion and biocompatible characteristics on nanopaper in comparison to conventional plastic labware. Confluency of HUVECs after 48 h of culture was measured under four different substrate conditions (Fig. 6a–h). HUVEC confluency on the pristine nanopaper (23.8%) was significantly lower than that of the uncoated polystyrene (PS) surface (56.6%) (Fig. 6i). However, after the nanopaper surface was coated with fibronectin (FN), confluency was significantly increased (48.2%) (Fig. 6j). Noticeably, with a slight decrease of confluency compared with FN-coated PS surface (58.2%), the confluency of FN-coated nanopaper showed no significant difference with that of FN-coated PS surface ( $P < 0.05$ , Fig. 6j), proving that the nanopaper has the potential to serve as a substrate for protein adsorption and cell culture. Thereafter, a basic cell culture experiment in the hollow channel of nanoFACES was subsequently performed to show how a paper-based substrate can be employed as a device material for microfluidic cell culture. HUVECs were cultured for 12 h in the hollow channel and viability remained high for the entire 12 h experiment (Figure 6j ii). HUVECs spread on the nanopaper channel surface and showed typical actin filament structures (Figure 6j i and iii–v). During experiments, nanoFACES were able to withstand 12 h of contact with cell culture media and repeated pipetting steps during the staining procedure. The use of collagen gel as the “adhesive” matrix helped to eliminate the need for any non-biocompatible adhesive bonding chemicals and ensured improved device integrity over the 12 h period. We also observed that the collagen helped to maintain flat nanopaper layers with minimal warping, which is a commonly observed problem when exposing nanopaper to aqueous solutions for extended periods of time. This demonstration of cell culture provides evidence that the nanoFACES could be a low-cost, biocompatible, and biodegradable choice of substrate material for biomicrofluidic device applications, with potential to further

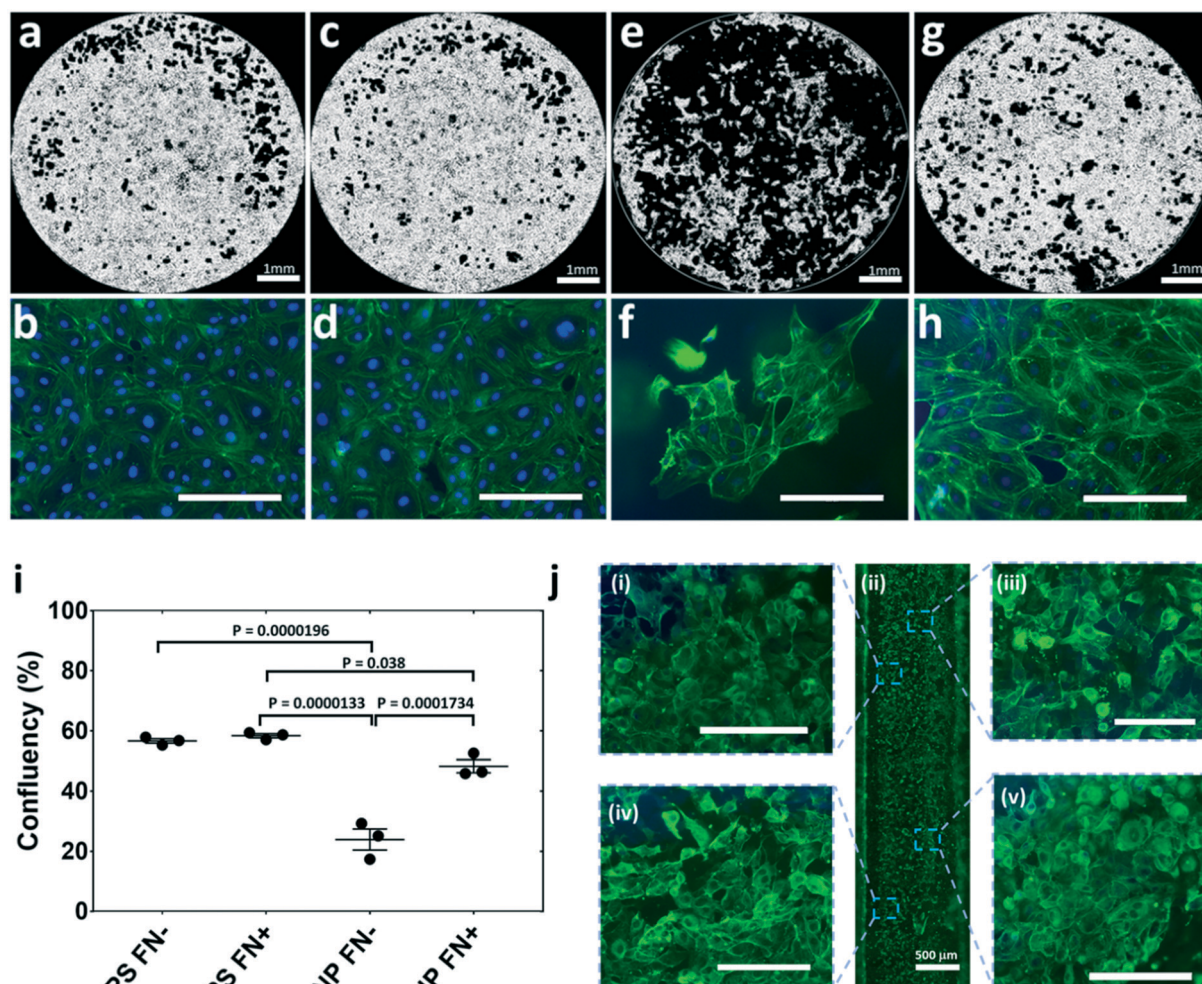


**Fig. 6** NanoFACES for microfluidic cell culture of HUVECs. The HUVEC confluency was measured after 48 h from initial seeding. (a and b) Confluency of HUVECs in the 96-well surface with no fibronectin coating (PS FN-). (c and d) Confluency of HUVECs in the 96-well surface with fibronectin coating (PS FN+). (e and f) Confluency of HUVECs on the nanopaper with no fibronectin coating (NP FN-). (g and h) Confluency of HUVECs on nanopaper with fibronectin coating (NP FN+). (i) The confluency data under the four culture conditions, which was derived from the measurement of percentage area covered by the HUVECs. (j) HUVEC culture in the hollow channel of a nanoFACE. Panel (ii) shows the hollow channel with HUVECs after 12 h of initial seeding. Panels (i) and (iii-v) are magnified images showing morphology of the HUVECs at different locations of the hollow channel. Green: F-actin. Blue: Hoechst. Scale bar on magnified images: 200  $\mu$ m.

advance a Design for Sustainability (DfS) approach to biology research.<sup>68</sup>

## Conclusions

In summary, a novel transparent, pump-free and hollow-channel nanopaper device, branded as nanoPADs (for analytical testing) and nanoFACES (for cell culture), was developed by using laser-cut nanopaper layers as the device substrates and by using EVA or collagen as the bonding material. Importantly, the current device design enabled pump-free liquid transfer. The flow wicking performance within hollow channels was characterized under different channel sizes, providing guidelines for flow speed adjustment. Consequently, colorimetric glucose detection and SERS-based chemical sensing were demonstrated on the nanoPADs and on-chip HUVEC cell culture was demonstrated

on the nanoFACES. This nanopaper-based platform technology will significantly broaden the application of paper-based devices in the areas of bioanalysis and cell biology.

## Author contributions

B. Y. designed and manufactured the devices, conducted the characterization and bioanalysis experiments, analyzed the data and wrote the manuscript. S. P. conducted the cell culture experiments, analyzed the data and wrote the manuscript sections related to cell culture. L. C. conducted the mechanical characterization and SERS sensing experiments, and analyzed the data. X. D. wrote the codes for fluidic speed characterization. E. W. K. Y. conceived and supervised the cell culture experiments and contributed to the writing and editing of the manuscript. X. L. conceived and supervised the project and contributed to the writing and editing of the manuscript.

## Conflicts of interest

There are no conflicts to declare.

## Acknowledgements

The authors gratefully acknowledge the support from the Natural Sciences and Engineering Research Council of Canada (grant numbers: RGPIN-06374-2017 and RGPAS-507980-2017 to X. L. and RGPIN-05885-2019 to E. W. K. Y.), the EMHSeed Program of the University of Toronto, the Canada Foundation for Innovation (JELF-32171, JELF-37812), and the Chinese Scholarship Council (to X. D.). The authors also thank Mr. Sina Kheiri for the assistance on schematic figure rendering, Mr. Teng Cui for the technical assistance on AFM experiment, and Mr. Zhen Yin for the technical assistance on paper lamination protocols, and Dr. Hang Zhou for the discussion on the absorption of nanomaterial.

## References

- 1 A. W. Martinez, S. T. Phillips, M. J. Butte and G. M. Whitesides, *Angew. Chem., Int. Ed.*, 2007, **46**, 1318–1320.
- 2 X. Li, D. R. Ballerini and W. Shen, *Biomicrofluidics*, 2012, **6**, 011301.
- 3 A. K. Yetisen, M. S. Akram and C. R. Lowe, *Lab Chip*, 2013, **13**, 2210–2251.
- 4 Y. Yang, E. Noviana, M. P. Nguyen, B. J. Geiss, D. S. Dandy and C. S. Henry, *Anal. Chem.*, 2017, **89**, 71–91.
- 5 M. M. Gong and D. Sinton, *Chem. Rev.*, 2017, **117**, 8447–8480.
- 6 R. Derda, A. Laromaine, A. Mammoto, S. K. Tang, T. Mammoto, D. E. Ingber and G. M. Whitesides, *Proc. Natl. Acad. Sci. U. S. A.*, 2009, **106**, 18457–18462.
- 7 R. Derda, S. K. Tang, A. Laromaine, B. Mosadegh, E. Hong, M. Mwangi, A. Mammoto, D. E. Ingber and G. M. Whitesides, *PLoS One*, 2011, **6**, e18940.
- 8 J. P. Rolland and D. A. Mourey, *MRS Bull.*, 2013, **38**, 299–305.
- 9 D. M. Cate, J. A. Adkins, J. Mettakoonpitak and C. S. Henry, *Anal. Chem.*, 2015, **87**, 19–41.
- 10 A. W. Martinez, S. T. Phillips, G. M. Whitesides and E. Carrilho, *Anal. Chem.*, 2010, **82**, 3–10.
- 11 X. Li, C. Zhao and X. Liu, *Microsyst. Nanoeng.*, 2015, **1**, 1–7.
- 12 X. Li and X. Liu, *Adv. Healthcare Mater.*, 2016, **5**, 1326–1335.
- 13 H. Fu, P. Song, Q. Wu, C. Zhao, P. Pan, X. Li, N. Y. Li-Jessen and X. Liu, *Microsyst. Nanoeng.*, 2019, **5**, 1–12.
- 14 K. M. Schilling, A. L. Lepore, J. A. Kurian and A. W. Martinez, *Anal. Chem.*, 2012, **84**, 1579–1585.
- 15 D. M. Cate, J. A. Adkins, J. Mettakoonpitak and C. S. Henry, *Anal. Chem.*, 2014, **87**, 19–41.
- 16 A. C. Glavan, R. V. Martinez, E. J. Maxwell, A. B. Subramaniam, R. M. Nunes, S. Soh and G. M. Whitesides, *Lab Chip*, 2013, **13**, 2922–2930.
- 17 M. M. Thuo, R. V. Martinez, W.-J. Lan, X. Liu, J. Barber, M. B. Atkinson, D. Bandarage, J.-F. Bloch and G. M. Whitesides, *Chem. Mater.*, 2014, **26**, 4230–4237.
- 18 C. Renault, X. Li, S. E. Fosdick and R. M. Crooks, *Anal. Chem.*, 2013, **85**, 7976–7979.
- 19 C. Renault, M. J. Anderson and R. M. Crooks, *J. Am. Chem. Soc.*, 2014, **136**, 4616–4623.
- 20 C. Renault, J. Koehne, A. J. Ricco and R. M. Crooks, *Langmuir*, 2014, **30**, 7030–7036.
- 21 H. Mao, W. Wu, D. She, G. Sun, P. Lv and J. Xu, *Small*, 2014, **10**, 127–134.
- 22 H. Kim, I.-K. Lee, K. Taylor, K. Richters, D.-H. Baek, J. H. Ryu, S. J. Cho, Y. H. Jung, D.-W. Park and J. Novello, *Sci. Rep.*, 2018, **8**, 1–9.
- 23 M. M. Hamed, B. Ünal, E. Kerr, A. C. Glavan, M. T. Fernandez-Abedul and G. M. Whitesides, *Lab Chip*, 2016, **16**, 3885–3897.
- 24 M. Nogi, S. Iwamoto, A. N. Nakagaito and H. Yano, *Adv. Mater.*, 2009, **21**, 1595–1598.
- 25 H. Zhu, Z. Fang, C. Preston, Y. Li and L. Hu, *Energy Environ. Sci.*, 2014, **7**, 269–287.
- 26 L. Chen, B. Ying, P. Song and X. Liu, *Adv. Mater. Interfaces*, 2019, **6**, 1901346.
- 27 E. Morales-Narváez, H. Golmohammadi, T. Naghdi, H. Yousefi, U. Kostiv, D. Horak, N. Pourreza and A. Merkoçi, *ACS Nano*, 2015, **9**, 7296–7305.
- 28 F. Cheng, X. Cao, H. Li, T. Liu, X. Xie, D. Huang, S. Maharjan, H. P. Bei, A. Gómez and J. Li, *Nano Lett.*, 2019, **19**, 3603–3611.
- 29 A. Barhoum, P. Samyn, T. Öhlund and A. Dufresne, *Nanoscale*, 2017, **9**, 15181–15205.
- 30 H. Sehaqui, T. Zimmermann and P. Tingaut, *Cellulose*, 2014, **21**, 367–382.
- 31 K. M. A. Uddin, V. Jokinen, F. Jahangiri, S. Franssila, O. J. Rojas and S. Tuukkanen, *Global Challenges*, 2019, **3**, 1800079.
- 32 S. Shin and J. Hyun, *ACS Appl. Mater. Interfaces*, 2017, **9**, 26438–26446.
- 33 C. D. Kelman and D. P. DeVore, *US Pat.*, 5219895, 1993.
- 34 P. Heher, J. Ferguson, H. Redl and P. Slezak, *Expert Rev. Med. Devices*, 2018, **15**, 747–755.
- 35 P. Ferreira, H. Gil and P. Alves, in *Recent advances in adhesions research*, ed. A. McFarland and M. Akins, Nova Science Publishers Inc., New York, 2013, pp. 59–85.
- 36 M. J. Buckley and E. J. Beckman, *Oral and Maxillofacial Surgery Clinics*, 2010, **22**, 195–199.
- 37 D. Erdogan, W. De Graaf and T. Van Gulik, *Eur. Surg. Res.*, 2008, **41**, 298–302.
- 38 J. T. Lu, C. J. Lee, S. F. Bent, H. A. Fishman and E. E. Sabelman, *Biomaterials*, 2007, **28**, 1486–1494.
- 39 G. Pagano, M. Ventre, M. Iannone, F. Greco, P. Maffettone and P. Netti, *Biomicrofluidics*, 2014, **8**, 046503.
- 40 J. Xie, J. Y. Lee and D. I. Wang, *Chem. Mater.*, 2007, **19**, 2823–2830.
- 41 X. Li and X. Liu, *Microfluid. Nanofluid.*, 2014, **16**, 819–827.
- 42 C. Zhao, M. M. Thuo and X. Liu, *Sci. Technol. Adv. Mater.*, 2013, **14**, 054402.
- 43 T. Brooks and C. Keevil, *Lett. Appl. Microbiol.*, 1997, **24**, 203–206.
- 44 T. Saito, S. Kimura, Y. Nishiyama and A. Isogai, *Biomacromolecules*, 2007, **8**, 2485–2491.

- 45 T. Saito and A. Isogai, *Biomacromolecules*, 2004, **5**, 1983–1989.
- 46 A. Isogai, T. Saito and H. Fukuzumi, *Nanoscale*, 2011, **3**, 71–85.
- 47 H. Fukuzumi, T. Saito, Y. Okita and A. Isogai, *Polym. Degrad. Stab.*, 2010, **95**, 1502–1508.
- 48 X. Yang, M. S. Reid, P. Olsén and L. A. Berglund, *ACS Nano*, 2019, **14**, 724–735.
- 49 H. Zhu, Z. Xiao, D. Liu, Y. Li, N. J. Weadock, Z. Fang, J. Huang and L. Hu, *Energy Environ. Sci.*, 2013, **6**, 2105–2111.
- 50 ASTM F1980-16, *Standard Guide for Accelerated Aging of Sterile Barrier Systems for Medical Devices*, ASTM International, West Conshohocken, PA, 2016, www.astm.org.
- 51 J. Huang, H. Zhu, Y. Chen, C. Preston, K. Rohrbach, J. Cumings and L. Hu, *ACS Nano*, 2013, **7**, 2106–2113.
- 52 H. Zhu, W. Luo, P. N. Ciesielski, Z. Fang, J. Zhu, G. Henriksson, M. E. Himmel and L. Hu, *Chem. Rev.*, 2016, **116**, 9305–9374.
- 53 M. Österberg, J. Vartiainen, J. Lucenius, U. Hippi, J. Seppälä, R. Serimaa and J. Laine, *ACS Appl. Mater. Interfaces*, 2013, **5**, 4640–4647.
- 54 R. Weishaupt, G. Siqueira, M. Schubert, P. Tingaut, K. Maniura-Weber, T. Zimmermann, L. Thöny-Meyer, G. Faccio and J. Ihssen, *Biomacromolecules*, 2015, **16**, 3640–3650.
- 55 C. Fritz, B. Jeuck, C. Salas, R. Gonzalez, H. Jameel and O. J. Rojas, in *Cellulose Chemistry and Properties: Fibers, Nanocelluloses and Advanced Materials*, Springer, 2015, pp. 207–224.
- 56 Z. Yin, F. Hannard and F. Barthelat, *Science*, 2019, **364**, 1260–1263.
- 57 Z. Yin, A. Dastjerdi and F. Barthelat, *Acta Biomater.*, 2018, **75**, 439–450.
- 58 R. Masoodi and K. M. Pillai, *Wicking in porous materials: traditional and modern modeling approaches*, CRC Press, Boca Raton, FL, 2012, pp. 31–53.
- 59 C. K. Camplisson, K. M. Schilling, W. L. Pedrotti, H. A. Stone and A. W. Martinez, *Lab Chip*, 2015, **15**, 4461–4466.
- 60 A. D. S. Indrasekara, S. Meyers, S. Shubeita, L. C. Feldman, T. Gustafsson and L. Fabris, *Nanoscale*, 2014, **6**, 8891–8899.
- 61 H. Orelma, I. Filpponen, L.-S. Johansson, M. Österberg, O. J. Rojas and J. Laine, *Biointerphases*, 2012, **7**, 61–72.
- 62 B. Liu and J. Liu, *Matter*, 2019, **1**, 825–847.
- 63 H. Pu, W. Xiao and D.-W. Sun, *Trends Food Sci. Technol.*, 2017, **70**, 114–126.
- 64 I. Jahn, O. Žukovskaja, X.-S. Zheng, K. Weber, T. Bocklitz, D. Cialla-May and J. Popp, *Analyst*, 2017, **142**, 1022–1047.
- 65 S. A. Ogundare and W. E. Van Zyl, *Cellulose*, 2019, **26**, 6489–6528.
- 66 J. Langer, D. Jimenez de Aberasturi, J. Aizpurua, R. A. Alvarez-Puebla, B. Auguie, J. J. Baumberg, G. C. Bazan, S. E. Bell, A. Boisen and A. G. Brolo, *ACS Nano*, 2020, **14**, 28–117.
- 67 Z. Huang, A. Nagpal, S. Siddhanta and I. Barman, *J. Raman Spectrosc.*, 2018, **49**, 1552–1558.
- 68 A. M. Wan, D. Devadas and E. W. Young, *Sens. Actuators, B*, 2017, **253**, 738–744.